ACS Catalysis

Research Article

pubs.acs.org/acscatalysis

Role of Interface Contact in CeO_2–TiO_2 Photocatalytic Composite Materials

Mario J. Muñoz-Batista,[†] María Natividad Gómez-Cerezo,[†,‡] Anna Kubacka,*[,†] David Tudela,[‡] and Marcos Fernández-García*[,†]

[†]Instituto de Catálisis y Petroleoquímica, CSIC, C/Marie Curie 2, 28049 Madrid, Spain

[‡]Departamento de Química Inorgánica, Facultad de Ciencias, Universidad Autónoma de Madrid, Campus Cantoblanco, 28049 Madrid, Spain

Supporting Information

ABSTRACT: The role of interface contact between two oxides, CeO_2 and TiO_2, for the photocatalytic elimination of toluene is examined in a series of samples with variable quantities of ceria. Samples having ceria contents in the 1 to 10 mol % range improve significantly, exhibiting up to 3.5 times the activity of the bare nano-TiO_2 catalyst. To interpret the photocatalytic behavior, this contribution develops a novel spectro-kinetic approach where a joined analysis of the kinetics of the reaction and the fate of charge carriers is merged with the mathematical modeling of the light–catalyst interaction at the photoreactor. This produces a self-consistent approach that simultaneously validates the kinetic model and interprets the activity on rigorous bases. The study is completed with a multitechnique examination of the solids using X-ray diffraction and electron paramagnetic resonance, UV–vis, and X-ray photoelectron spectroscopies as well as high-resolution transmission electron microscopy. The results provide quantitative evidence that the oxide–oxide contact controls the photoactivity through the number of hole-related species available at the surface of the composite materials and that this number is in turn related to the stabilization of reduced Ce species present at the Ce–Ti interface.

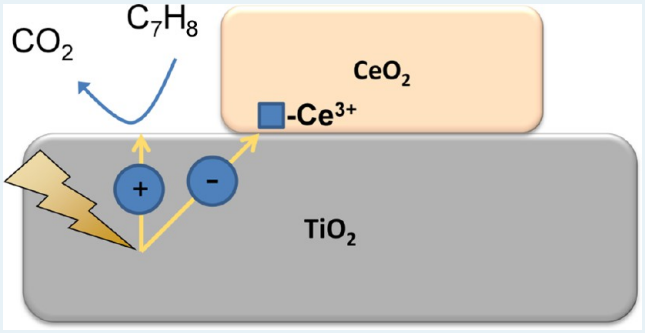

KEYWORDS: *anatase, ceria, spectro-kinetic study, degradation, pollutant*

I. INTRODUCTION

Heterogeneous photocatalysis by nanocrystalline semiconductors is an exciting technology applied to abatement of pollutants in both liquid and gas phases. This is essentially based in the excellent performance and stability of titania, the most prominent photocatalytic material, for the mineralization of typical pollutants, including refractory or non-biodegradable molecules, under mild conditions, such as room temperature and atmospheric pressure and using oxygen (air) as the oxidizing agent.[1−4] Among titania single nanophases, anatase is clearly the most active phase, largely because it shows a correct balance between its surface-chemistry-related properties and the adequate physical properties for efficient handling of light-triggered charge carriers, allowing them to be involved in chemical steps at the surface.[4]

Nevertheless, the activity of the anatase phase needs further improvement in order to produce robust systems with wide application for complete degradation of all kind of pollutants as well as to be able to work under all kinds of experimental conditions. Such a general objective has been accomplished by a number of different approaches. Almost from the beginning of the field of photocatalysis, anatase-TiO_2 modification by anion–cation (co)doping[1−14] or coupling of anatase-TiO_2 with *other* semiconductors (including other titania polymorphs)[1−4,15−24] as well as metals[1−4,25−30] has been pursued in this quest. Among composite systems with titania, cerium oxide appears as a useful candidate for several reasons. First, ceria (CeO_2) itself is an active system in the photodegradation of several molecules.[31−33] Second, its combination with titania has been proved to be effective in numerous degradation or redox photoreactions.[34−38] The positive effect observed in composite systems is supposed to be a combination of factors related to the modification of the surface as well as the optical and charge-handling properties owned by the nanocomposites with respect to those displayed by the single-phase anatase reference material.

In the present work, we used the CeO_2–TiO_2 system as a prototypical system where the oxide–oxide interaction results in beneficial effects, boosting the performance of the anatase material significantly. Among all works published previously in the CeO_2–TiO_2 system, not a single one has reported a negative effect.[34−38] However, the understanding of the system

Received: October 4, 2013
Revised: November 26, 2013
Published: November 27, 2013

   dx.doi.org/10.1021/cs400878b | ACS Catal. 2014, 4, 63−72

is far from reaching a point where a basic interpretation of the key phenomena driving the photoactivity has been fully achieved. To shed some light on the problem, we scanned the physicochemical and catalytic properties of the contact between the two oxides as a function of the molar content of ceria. Within such a framework, this contribution develops a novel spectro-kinetic approach where a joined analysis of the kinetics of the reaction and the fate of charge carriers is merged with mathematical modeling of the light−catalyst(s) interaction at the photoreactor. Specifically, we confront the photoelimination rate of the materials as a function of the kinetic constants obtained by (kinetic) modeling with the results obtained though electron paramagnetic resonance (EPR) analysis of the series of samples and relate it to the rate of formation of surface-radical-producing chemistry. This provides a self-consistent approach that simultaneously validates the kinetic model and interprets the activity on rigorous bases, the latter by uncovering the key physicochemical phenomena involved in the kinetically relevant steps. The study is completed with a multitechnique examination of the solid using X-ray diffraction (XRD) and X-ray photoelectron spectroscopy (XPS) as well as high-resolution transmission electron microscopy (HRTEM). The unique chemical nature of the composite systems is evidenced from the whole study and the chemical consequences of the ceria − titania contact for the photoelimination of toluene are clarified. Toluene photomineralization was chosen to test activity as it is thought to be an important constituent of anthropogenic emissions in urban atmospheres. Additionally, its photo-oxidation is a very demanding reaction and thus constitutes a tough chemical test to assess the potential of the TiO_2-based systems in the photoelimination of organic pollutants.[39,40]

II. EXPERIMENTAL SECTION

Catalyst Preparation. Materials were obtained by means of a microemulsion preparation method utilizing *n*-heptane (Scharlau) as an organic medium, Triton X-100 (Aldrich) as a surfactant, and hexanol (Aldrich) as a cosurfactant. A TiO_2 reference sample was obtained as a first step using a water-in-oil microemulsion and titanium tetraisopropoxide as the precursor. In all of the composite samples and the CeO_2 reference, cerium(III) nitrate (Alfa Aesar) was introduced into the aqueous phase of the microemulsion. After 30 min of stirring, the stoichoimetric quantity of tetramethylammonium hydroxide (TMAH) needed to obtain the corresponding Ce(III) hydroxide was introduced from the aqueous phase of a similar microemulsion under stirring for ca. 5 min. For nanocomposite samples, a titanium tetraisopropoxide solution in isopropanol (2:3) was subsequently added dropwise to the Ce-containing microemulsion. The water/M (M = Ti, Ce, or Ce + Ti) and water/surfactant molar ratios were 110 and 18, respectively, for all samples.[41,42] The resulting mixture was stirred for 24 h and then centrifuged, and the separated solid precursors rinsed with methanol and dried at 110 °C for 12 h. After drying, the solid precursors were subjected to a heating ramp (2 °C min^{-1}) up to 500 °C, after which this temperature was maintained for 2 h. Sample names are Ti and Ce for the titania and ceria references, respectively, and *x*CeTi for the composite ones, where *x* is the Ce/Ti molar ratio.

Characterization Details. The Brunauer−Emmett−Teller (BET) surface areas and average pore volumes and sizes were measured by nitrogen physisorption (Micromeritics ASAP 2010). The Ce/Ti composition was analyzed by using inductively coupled plasma atomic absorption spectroscopy (ICP-AAS) (PerkinElmer Optima 3300 DV). UV−vis transmission or diffuse-reflectance spectroscopy experiments were performed with a Shimadzu UV2100 apparatus using, for diffuse experiments, $BaSO_4$ as a reference. A summary of the morphological and structural properties of the samples included in this work is presented in Table 1.

Table 1. Sample Chemical Compositions and Morphological Properties[a]

sample	Ce/Ti TXRD	BET surface area (m^2 g^{-1})	pore volume (cm^3 g^{-1})	pore size (nm)	porosity (%)
Ti	–	113.5	0.236	8.31	47.9
0.01CeTi	0.02	83.5	0.138	6.17	35.0
0.025CeTi	0.03	78.0	0.136	6.12	35.7
0.05CeTi	0.06	75.5	0.129	6.83	34.4
0.1CeTi	0.12	77.2	0.096	4.60	27.2
0.25CeTi	0.30	108.8	0.148	5.39	42.6

[a]Standard errors: Ce/Ti, 0.01; BET, 1.5 m^2 g^{-1}; porosity, 8%.

XRD profiles were obtained on beamline ID15A at the European Synchrotron Radiation Facility (ESRF). Diffraction measurements were collected at 69.525 keV with a digital flat 2D panel detector (Pixium 4700) located 1100 mm from the sample position and fitted using the Rietveld formalism with the XPert Highscore Plus program (Panalytical). Particle sizes were measured with XRD using the Williamson−Hall formalism.[43]

XPS data were recorded on 4 mm × 4 mm pellets with a thickness of 0.5 mm prepared by slightly pressing powered materials that had been outgassed in the prechamber of the instrument at room temperature at a pressure of $<2 \times 10^{-8}$ Torr to remove chemisorbed water from their surfaces. The SPECS spectrometer main chamber, working at a pressure $<10^{-9}$ Torr, was equipped with a PHOIBOS 150 multichannel hemispherical electron analyzer with a dual X-ray source working with Al Kα radiation ($h\nu$ = 1486.2 eV) at 120 W, 20 mA using C 1s (284.6 eV) as the energy reference. Surface chemical compositions were estimated from the XPS spectra by calculating the integral of each peak after subtraction of the "S-shaped" Shirley-type background using the appropriate experimental sensitivity factors by means of CASAXPS software (version 2.3.15). The analysis of the Ce $3d_{5/2}$ peak was carried out following procedures summarized by Paparazzo.[44]

HRTEM and X-ray energy-dispersive spectroscopy (XEDS) were performed using a JEOL 2100F TEM/STEM microscope. XEDS analysis was performed in scanning TEM (STEM) mode with a probe size of ∼1 nm using the INCA x-sight detector (Oxford Instruments). Specimens were prepared by depositing particles of the samples to be investigated onto a copper grid supporting a perforated carbon film. Deposition was achieved by dipping the grid directly into the powder of the samples to avoid contact with any solvent.

The EPR measurements were done with a Bruker ER200D spectrometer operating in the X band and calibrated with a 2,2-diphenyl-1-picrylhydrazyl (DPPH) standard. For the 5,5-dimethyl-1-pyrroline *N*-oxide (DMPO) spin-trapping EPR experiments, the samples were suspended in water at a concentration of 0.6 g L^{-1} and sonicated for 4 min. A 0.01 M aqueous solution of the DMPO spin trap (supplied by Sigma) was prepared and kept on ice during the whole set of

dx.doi.org/10.1021/cs400878b | ACS Catal. 2014, 4, 63−72

experiments. Bidistilled water (Elix-10) was employed for these preparations. The solid suspension (100 μL) and the DMPO solution (100 μL) were mixed into an EPR flat quartz cell under atmospheric air and irradiated for different times through a spectroscopic Pyrex glass filter with a cutoff at ca. 220 nm using a light excitation source identical to that employed for the photokilling tests. The cell was then immediately transferred to the spectrometer cavity for EPR analysis. A small decay of the radical concentration (ca. 5% on average) was observed in the dark during the course of spectrum recording. The spectra were obtained at 298 K at a microwave frequency of ca. 9.75 GHz, a microwave power of 19.5 mW, a modulation frequency of 100 kHz, a modulation amplitude of 1 G, and a spectrometer gain of 2×10^5. No significant signal saturation was observed under those conditions. Blank experiments were also performed over mixtures of 100 μL of the DMPO solution and 100 μL of water to confirm the absence of radical formation in the absence of the solid under the employed conditions.

Reaction System. Gas-phase photooxidation tests were carried out with toluene using a setup described in the Supporting Information. The gas-phase photooxidation was tested in a continuous-flow annular photoreactor containing ca. 40 mg of photocatalyst as a thin-layer coating on a Pyrex tube. The corresponding amount of catalyst was suspended in 1 mL of ethanol, painted on a Pyrex tube (cutoff at ca. 290 nm), and dried at room temperature. The reacting mixture (100−300 $cm^3\ min^{-1}$) was prepared by injecting toluene (≥99%; Aldrich) into a wet [ca. 90% relative humidity (RH)] 20 vol % O_2/N_2 flow before it entered the photoreactor, yielding an organic inlet concentration in the range 100−700 ppmv. After the mixture was flowed for 6 h in the dark (control test), the catalyst was irradiated using four fluorescent UV lamps (Sylvania F6WBLT-65, 6 W) symmetrically positioned outside the photoreactor. The concentrations of reactants and products were analyzed using an online gas chromatograph (Agilent GC 6890) equipped with HP-PLOT-Q/HP-Innowax columns (0.5/0.32 mm I.D. × 30 m) and thermal conductivity and flame ionization detectors.

III. RESULTS AND DISCUSSION

III.1. Characterization Results. In Figure 1 we have plotted the XRD patterns of the TiO_2 reference sample and *x*CeTi composites. The well-known anatase (JCPDS card no. 78-2486, corresponding to the $I4_1/amd$ space group) and fluorite CeO_2 (JCPDS card no. 87-0792, corresponding to the $Fm3m$ space group) structures are easily observed. A minor peak at ca. 2.18 $Å^{-1}$ points to the presence of minute quantities (below 1.5 vol % for all samples) of brookite (JCPDS card no. 76-1937, corresponding to the *Pbca* space group). The composite samples always displayed the presence of the anatase phase, but fluorite CeO_2 was detected only for samples with a Ce content equal to or above that of the 0.05CeTi specimen. In these materials, anatase had a primary particle size of ca. 12−15 nm, while fluorite, when detected, had a primary particle size of ca. 5.0−9.5 nm (Table 2).

It can be also mentioned that significant anatase doping by ceria was absent, as shown by the constancy of the anatase cell volume (the XRD-derived cell volume ranged from 136.1 to 136.4 $Å^3$ for all of the samples), indicating that Ce is primarily at the surface of the anatase phase in these materials. The preparation method favors such a structural situation, as the Ce component is precipitated before contact with titania occurs. The concomitant analysis of porosity (Table 1) indicates that

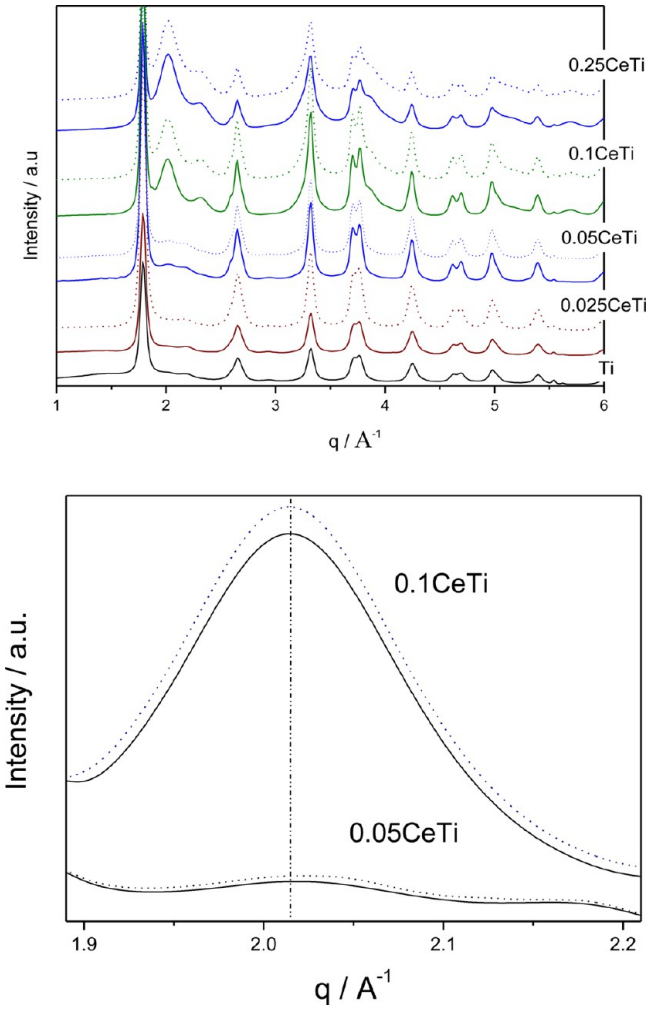

Figure 1. Upper panel: XRD diffractograms of the Ti reference and *x*CeTi samples. The pattern for the 0.01CeTi sample has been omitted because it showed no significant differences with that of 0.025CeTi (only anatase peaks were discernible). For each *x*CeTi sample, two patterns are presented, corresponding to fresh (solid line) and spent (after reaction; dashed line) samples. Lower panel: detail of the most intense ceria peak for selected samples.

Table 2. XRD-Derived Parameters for the Ti Reference and *x*CeTi Samples[a]

	size (nm)		cell parameters (Å)		
			TiO_2 anatase		CeO_2 fluorite
sample	TiO_2	CeO_2	*a*	*b*	*a*
Ti	12.1	–	3.787	9.488	–
0.01CeTi	13.0	–	3.790	9.488	–
0.025CeTi	13.2	–	3.792	9.490	–
0.05CeTi	15.0	5.3	3.788	9.491	5.426
0.1CeTi	15.0	9.4	3.789	9.495	5.412
0.25CeTi	15.2	8.5	3.790	9.496	5.413

[a]Standard errors: size, 0.5 nm; cell parameters, 0.003 Å.

small CeO_x clusters tend to be located in the anatase pores, partially occluding them, for samples with ceria content below or equal to that of 0.1CeTi. In samples with higher ceria content, a significant part of the ceria forms fluorite-type particles with enough size to have loose contact with titania. Such ceria nanoparticles generate a high-surface-area compo-

dx.doi.org/10.1021/cs400878b | ACS Catal. 2014, 4, 63−72

nent, increasing this observable in the composite material as well as reversing the porosity trend detected for the samples with lower Ce content (Table 1). Together with the XRD data concerning fluorite-CeO_2 particle size, the morphology data suggest that the loose-contacting ceria nanoparticles correspond to the main Ce-containing component of the 0.1CeTi and 0.25CeTi catalysts. This fluorite component is thus responsible for the differential morphological characteristics with respect to the samples with low Ce content. The cutoff between low and high Ce content zones is not well-defined but certainly occurs between the 0.05CeTi and 0.1CeTi samples.

The structural and morphological study was completed with the help of microscopy tools. As shown in Figure 2, general

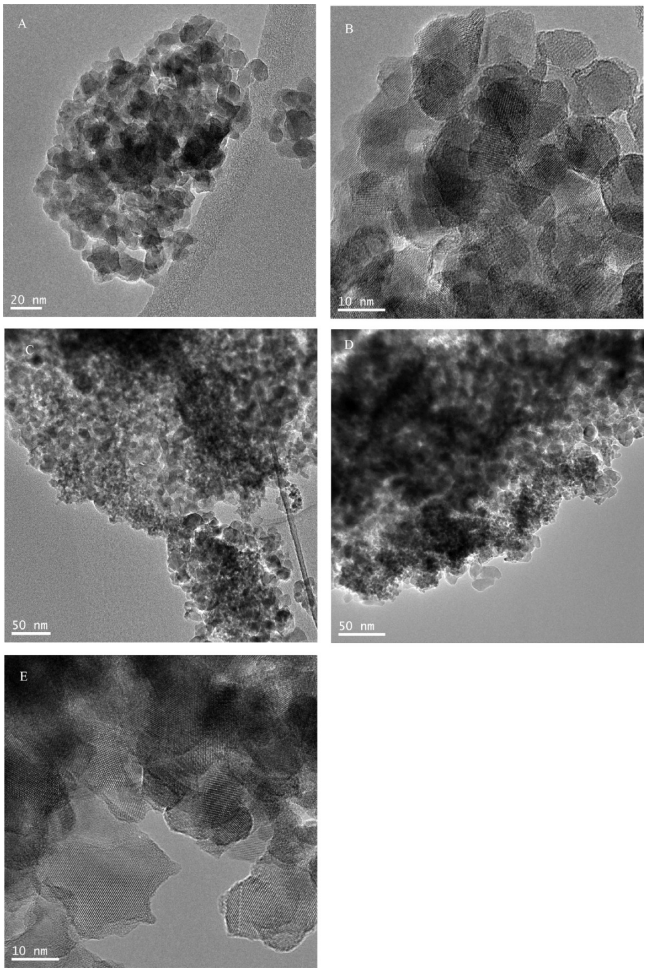

Figure 2. TEM views of (A, B) 0.05CeTi and (C–E) 0.25CeTi samples.

views of the 0.05CeTi and 0.25 CeTi catalysts allowed the intimate mixing of the two oxides to be visualized. Dark zones are Ce-rich (as confirmed by XEDS; see below) and appeared in all agglomerates analyzed. Both low- and high-resolution images provide evidence of the different morphologies of the two oxides; platelet-like TiO_2 particles are observed in intimate mixing with smaller, round-shaped CeO_2 particles. Ce is obviously more easily discerned in the 0.25CeTi sample. The spatial distribution of the two oxides was analyzed by XEDS (Figure 3). The TEM views presented in Figure 2 and the XEDS data presented in Figure 3 provide evidence of the heterogeneous distribution of the CeO_2 nanoparticles within

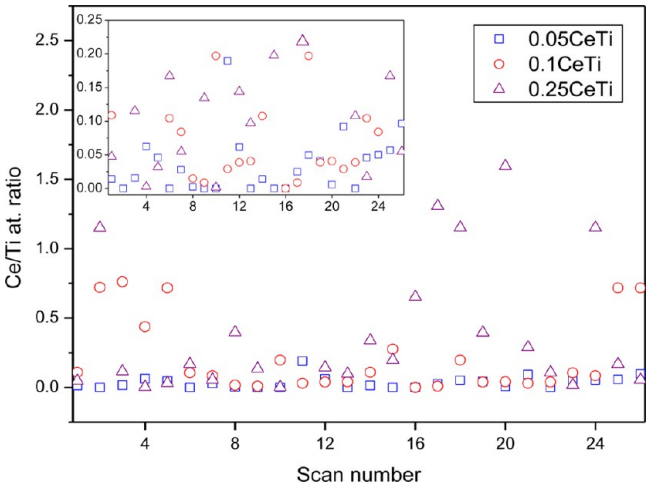

Figure 3. XEDS analysis of the Ce/Ti atomic ratio at several positions in the samples.

agglomerates predominantly formed by TiO_2, without significant differences throughout the sample series. Therefore, the TEM–XEDS analysis is in agreement with the results of the XRD study concerning the fact that smaller, round-shaped particles of CeO_2 are in contact with larger, platelet-type TiO_2 particles, but it also indicates significant heterogeneity in terms of the Ce/Ti ratio observed in different zones of the materials. Such a morphological issue was shared by all of the samples studied.

Additional information concerning the Ce dispersion behavior though the series is provided by a comparison of the Ce/Ti atomic ratios determined by TXRD (Table 1) and XPS (Table 3). The ratio of these ratios indicates again the presence of two "types" of samples corresponding to zones of low and high Ce loading. The XPS/TXRD ratio is above and below 2 for samples with low and high Ce loading, respectively, with a cutoff somewhere between the 0.05CeTi and 0.1CeTi samples. Below the cutoff, the ceria nanoparticles are in close contact with the titania surface region and may occlude its pores. This results in a shadowing or partial covering of the titania by the ceria component, as detected by the XPS/TXRD comparison. Above that point, bigger Ce particle size(s) and significantly lower oxide–oxide degrees of contact are observed, rationalizing the observed diminishing difference between the TXRD and XPS Ce/Ti atomic ratios.

The XRD study of the lattice parameters also showed some differences among our samples concerning structural parameters. Such differences concern the fluorite phase, which apparently has a visible difference in lattice constant for samples with high and low Ce contents (Figure 1 and Table 2). While the 0.1CeTi and 0.25CeTi samples do not exhibit significant differences, the 0.05CeTi sample presents an expanded fluorite lattice, corresponding to the presence of ca. 20% Ce^{3+}.[45,46] The presence of the reduced ceria state seems to be unequivocally connected with a low ceria content in the catalyst. To further support such point, an XPS study of the materials was carried out. The Ce 3d peaks of the materials are displayed in Figure 4, while a representative analysis of such contributions following the procedure described by Paparazzo[44] is presented in Figure 5 for the 0.25CeTi sample. A simple look at Figure 4 shows that the presence of reduced Ce states is common to all of the samples with low Ce content. It should be noted that according to XRD (Figure 1), the numbers of Ce^{3+}

dx.doi.org/10.1021/cs400878b | ACS Catal. 2014, 4, 63–72

Table 3. XPS Data for the *x*CeTi Series[a]

	binding energy (eV)												%		
	Ce $3d_{5/2}$					Ce $3d_{3/2}$									
sample	v_0 Ce(III)	v Ce(IV)	v′ Ce(III)	v″ Ce(IV)	v‴ Ce(IV)	u_0 Ce(III)	u Ce(IV)	u′ Ce(III)	u″ Ce(IV)	u‴ Ce(IV)	Ti $2p_{3/2}$	O 1s	Ce(III)	Ce(IV)	Ce/Ti_{XPS}
0.25CeTi	880.4	882.4	884.4	888.2	898.2	898.7	901.0	903.0	907.3	916.6	458.5	529.7	18.8	81.2	0.43
0.1CeTi	880.2	882.5	885.4	888.9	898.2	898.6	900.9	903.8	907.3	916.6	458.7	529.9	19.5	80.5	0.19
0.05CeTi	nf	882.3	884.8	888.5	898.3	nf	900.9	903.7	907.4	916.7	458.4	529.7	58.9	31.1	0.12
0.025CeTi	nf	882.6	885.2	888.6	898.5	nf	901.0	903.9	907.2	916.7	458.4	529.7	68.7	21.3	0.10
0.01CeTi	nf	882.1	885.3	888.4	898.4	nf	901.2	903.9	907.4	916.7	458.3	529.9	72.3	17.7	0.04_5

[a]"nf" = not fitted. Standard errors: binding energy, 0.2 eV; Ce molar content, 4%; Ce/Ti ratio, 0.02.

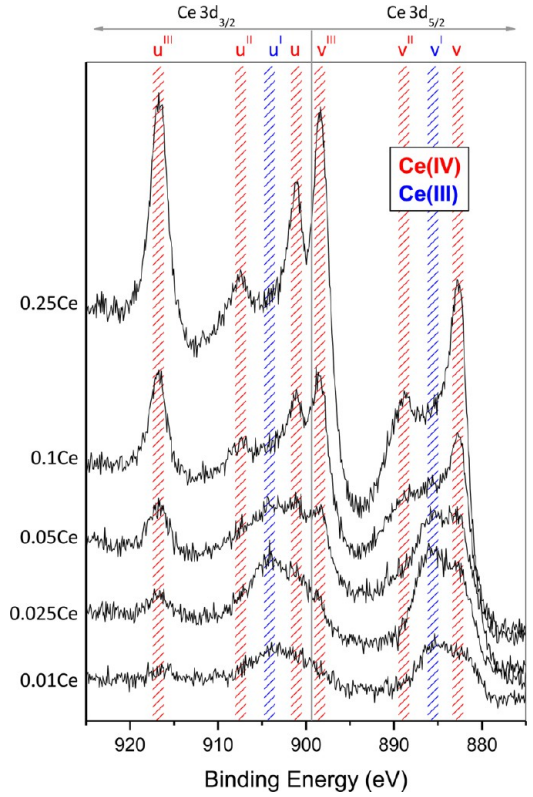

Figure 4. Ce 3d XPS spectra for the *x*CeTi samples. Regions where Ce^{3+} and Ce^{4+} contributions are dominant are highlighted in blue and red, respectively.

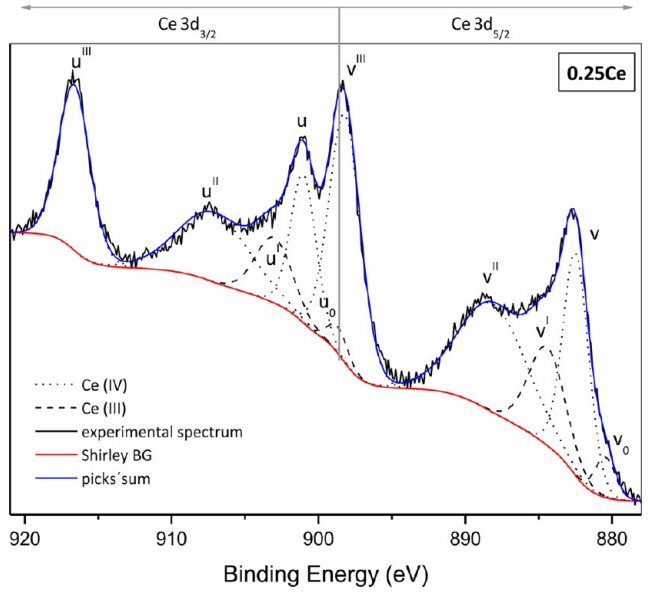

Figure 5. Representative example of the fitting procedure for the Ce $3d_{5/2}$ peak.

species in the fresh and spent samples are the same in going from 0.05CeTi to 0.25CeTi (i.e., in samples where the fluorite phase is detected). No further differences among the samples [e.g., Ti $2p_{3/2}$ binding energy at 458.5 ± 0.3 eV, characteristic of Ti(IV) species] were detected.

The quantitative analysis of the Ce 3d XPS peaks for the samples is summarized in Table 3. All of the Ce^{4+} and Ce^{3+} peaks in the 3d regions were assigned through their binding energies.[44,47] The percentages of Ce at the surface, as measured by the Ce/Ti ratio, and the percentages of the total Ce in the Ce^{3+} and Ce^{4+} states are also included in the table. The most important issue is related to the behavior of the Ce^{3+} content throughout the series. XPS detected this state for all of the samples, but a strong increase of this contribution was observed for samples with Ce/Ti ratios equal to or below 0.05. This point was suggested by XRD, although the quantity of Ce^{3+} detected by XPS is significantly larger, indicating the higher concentration of this state at the surface of the particles. Reduced states are typically observed at edge positions of the ceria nanoparticles.[48] However, for the same particle sizes presented in Table 2, single oxide ceria nanoparticles prepared by us previously using the same microemulsion procedure and calcined at the same temperature showed a Ce^{3+} content below 1.5 atom %.[31] To interpret the high quantity of Ce^{3+} detected here, we note that the Ce−Ti interface has recently been shown to strongly promote the existence of reduced Ce^{3+} states as a consequence of the electronic contact.[49] Therefore, the presence of important quantities of reduced Ce states should be unequivocally related to a stabilization effect produced at the boundary between the two oxides. For obvious reasons, this displays an acute ceria size dependence. It should also be noted that the behavior of the Ce^{3+} content included in Table 3 qualitatively tracks the XRD-derived information, as it suffers a significant change concomitant with the presence of larger ceria particles, for example, between the 0.05CeTi and 0.1CeTi samples. The loss of contact between Ce and Ti oxides would thus explain the behavior of Ce^{3+} though the sample series, and therefore, the Ce^{3+} content is a clear fingerprint for measuring the degree of contact.

Optical properties and particularly photon absorption are of capital importance to interpret photocatalytic behavior. Figure 6 displays the diffuse-reflectance UV−vis spectra of the samples. As expected from the characteristic spectra of the pure oxides, we observed a continuous increase of absorption in

dx.doi.org/10.1021/cs400878b | ACS Catal. 2014, 4, 63−72

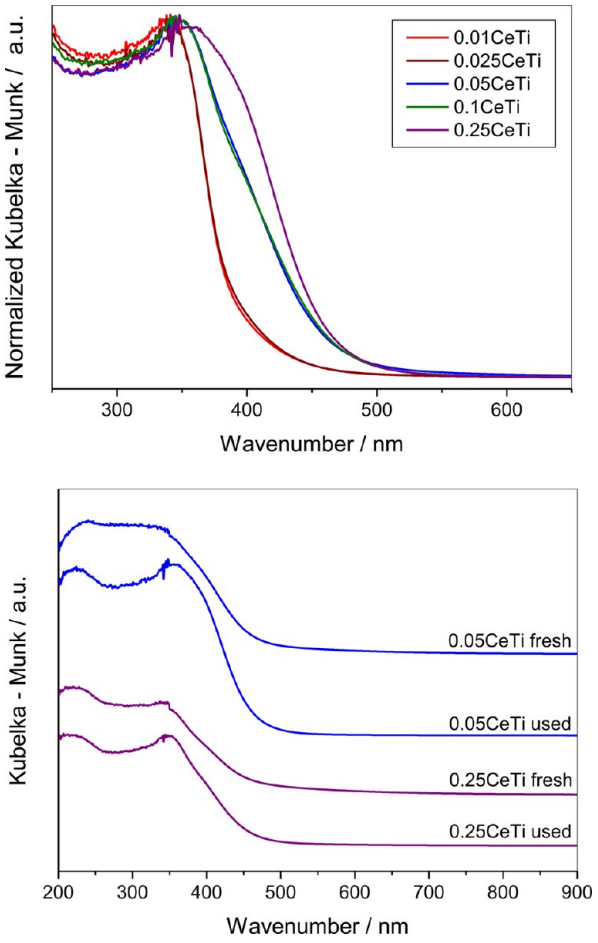

Figure 6. UV–vis spectra of the samples. Upper panel: Normalized (to enhance differences) spectra for *x*CeTi samples. Lower panel: spectra of fresh and spent 0.05CeTi and 0.25CeTi samples.

the visible region (going from ca. 380 to 500 nm) with increasing ceria content of the material.[33,50,51] This drives an apparent modification of the band gap, as presented in Table 4,

Table 4. Band Gaps of the Samples[a]

	band gap (eV)	
sample	fresh	spent
Ti	3.02	3.02
0.01CeTi	3.01	3.02
0.025CeTi	2.97	2.93
0.05CeTi	2.53	2.56
0.1CeTi	2.54	2.58
0.25CeTi	2.50	2.48

[a]Standard error: 0.05 eV.

which is obtained considering that the spectra are dominated by anatase, an indirect-gap semiconductor.[4] Bulk ceria must be an insulator, but nanomaterials typically display indirect-gap semiconductor behavior.[52,53] Our pure TiO_2 and CeO_2 references show band gaps of 3.02 eV (this work) and 2.55 eV (ref 32), respectively, and the TiO_2 value is included in Table 4. The band gaps go from 3.02 eV for pure anatase to ca. 2.50 eV for the 0.25CeTi sample. As observed by the previous techniques, the band-gap behavior through the series suffers more drastic changes around the 0.05CeTi sample. We stress that according to the previous characterization results, the band gaps can be understood as average values (taking into account the mass attenuation coefficient) of the corresponding pure oxides, the only two phases detected. Figure 6 also includes band gaps of some representative examples of spent (after reaction) materials. The UV–vis spectra display some differences attributable to surface states related to the presence of adsorbates/intermediates/residues produced during the reaction, but no important modification of the band gap was detected (Table 4).

III.2. Analysis of Photocatalytic Properties. A representative example of the catalytic performance in toluene photodegradation through the series of samples is presented in Figure 7. The reaction rate per unit surface area grows with the

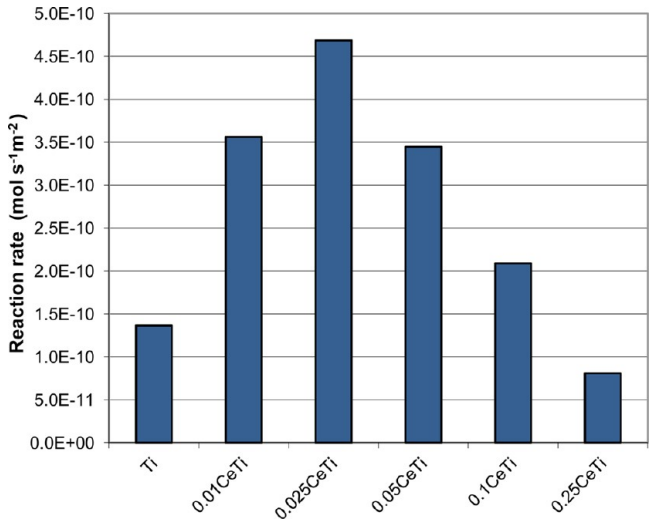

Figure 7. Surface-area-normalized reaction rate for toluene photooxidation (C_0 = 300 ppm, RH = 90%, T = 30 °C).

Ce content of the material up to the 0.025CeTi sample and then decays. Only in the 0.25CeTi case does Figure 7 display a rate below that corresponding to the Ti reference. The maximum activity increase is ca. 3.5 with respect to the titania reference. As P25 presents a slightly inferior activity than our Ti reference in toluene photodegradation,[7−9] the same conclusion holds for both titania-based reference systems. It should also be noted that ceria reference materials with particle sizes in the 5–10 nm range were previously tested by our group and showed rates ca. 1 order of magnitude inferior to that of the anatase reference system.[31] Therefore, an activity enhancement was observed with respect to both bare oxide references (particularly the anatase nanoreference). As mentioned above, the maximum of the activity enhancement is detected for relatively low Ce contents (2.5 mol %). This agrees with the literature, where optimum activity is usually observed at ceria contents below 10 mol %.[35,36,38]

To interpret the chemical behavior, we carried out a spectrokinetic analysis of the toluene photoelimination reaction. First, the influence of reactor space time (τ) on the toluene photodegradation (presented in Figure 8) was used to estimate the differences among samples in the formation of active radical species. More exactly, the fitting of the kinetic data displayed in Figure 8 was done according to eq 1 (see the Supporting Information for full details):

dx.doi.org/10.1021/cs400878b | ACS Catal. 2014, 4, 63−72

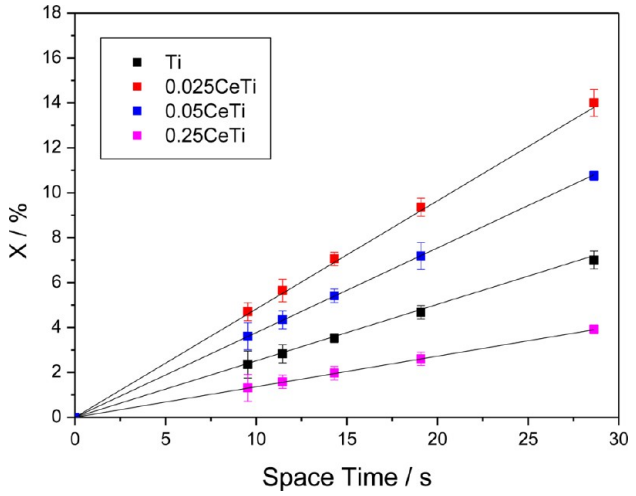

Figure 8. Effect of the space time on the toluene conversion (C_0 = 100 ppm, RH = 90%, T = 30 °C).

$$-\frac{1}{\alpha_1\sqrt{e^{a,s}}}[\log(1-X)+\alpha_2(-C_{C_6H_5CH_3,0}X)]=\tau \quad (1)$$

where $X = 1 - (C_{C_6H_5CH_3}/C_{C_6H_5CH_3,0})$ and $e^{a,s}$ is the local superficial rate of photon absorption (given by eq 21 in the Supporting Information). Equation 1 includes two parameters for each sample, α_1 and α_2, given by eqs 2 and 3, respectively:

$$\alpha_1=\sqrt{\frac{\bar{\phi}}{k_3}}\frac{k_4K_{C_6H_5CH_3}[\text{sites}]k_1[H_2O]_{ads}}{\gamma} \quad (2)$$

$$\alpha_2=\left(\frac{k_4[\text{sites}]}{\gamma}\right)K_{C_6H_5CH_3} \quad (3)$$

in which the k_j are kinetic constants for elementary reactions in the reaction scheme (Table S1 in the Supporting Information) and the other quantities are defined in the Supporting Information. The ratio of α_1 and α_2, denoted as α, is given by

$$\alpha=\frac{\alpha_1}{\alpha_2}=\sqrt{\frac{\bar{\phi}}{k_3}}k_1[H_2O]_{ads} \quad (4)$$

Under the experimental conditions used in the experiments (RH = 90%), the amount of adsorbed water is nearly constant, and thus, the α_1/α_2 ratio obtained from the fit (eq 4) provides information about the ratio of the rates of two elemental steps with kinetic constants k_1 and k_3. According to the model developed on the basis of Table S1 in the Supporting Information, step 1 is the creation of hole-related radicals while step 3 accounts for the annihilation of hole-related radicals. Such a procedure would thus render information about the availability of hole-related radical species during the reaction. Values of the fitting parameters α_1 and α_2 in eqs 2 and 3 are presented in Table 5. It should be noted that the error in α_2 from the analysis is relatively high for specific low-activity samples.

As a second step of the spectro-kinetic analysis, we used EPR spectroscopy to track the number of OH$^\bullet$ species at the surface of each sample (see the Supporting Information for details). With the help of a spin-trapping molecule, we measured the time evolution of the hole-related radical species (Figure 9). A comparison of the initial rates of OH$^\bullet$ formation for the first few minutes (before multiple additions, within consecutive

Table 5. Values of the Kinetic Parameters α_1 and α_2 and Their Ratio α Obtained from Fits of Equation 1

	Ti	0.025CeTi	0.05CeTi	0.25CeTi
α_1 (10^{-3} m^3 J^{-1})	0.7	8.4	1.6	0.4_5
α_2 (10^2 m^3 mol^{-1})	7.1	63.4	13.4	7.0
α (10^{-6} mol J^{-1})	0.99	1.32	1.19	0.64
$10^3 \times$ CI(α_1)^a	0.4	0.6	0.1	0.3
$10^{-2} \times$ CI(α_2)^a	6.1	4.8	1.0	6.9
$10^6 \times$ CI(α)^a	0.14	0.02	0.01_5	0.11

^{a}CI(z) denotes the 95% confidence interval of z in the appropriate units.

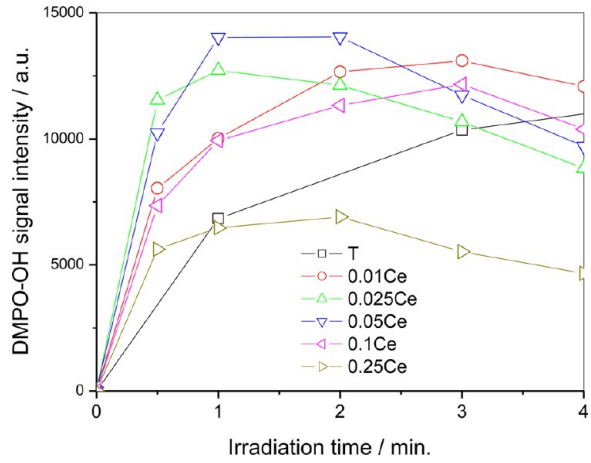

Figure 9. Time evolution of the DMPO−OH radical intensities in the presence of the Ti reference and the xCeTi samples.

reactions, of OH$^\bullet$ radicals to the spin-trapping molecule would lead to the formation of diamagnetic species) is customarily used to compare the abilities of the samples to generate this radical species.[9,38,54−56] According to the analysis carried out in the Supporting Information, this rate ($r_{OH^\bullet}$) is given by

$$\frac{r_{OH^\bullet}}{\sqrt{e^{a,s}}}=\sqrt{\frac{\bar{\phi}}{k_3}}k_1[H_2O]_{ads} \quad (5)$$

We can thus see that using either EPR kinetic analysis (normalized using the $e^{a,s}$ coefficient; for details, see the Supporting Information) or photocatalytic data, we can end up measuring the same physical observables (eqs 4 and 5). In Figure 10 we have used these two measurements with a twofold aim. First, the plot can be used to check the consistency of the approach used to obtain the above-mentioned quantitative interpretation. The correlation between these two parameters seems reasonably good. In fact, deviations between the two measurement techniques are only significant for the Ti and 0.25CeTi samples, the cases where the errors in the fitting parameters are significantly larger (see Table 5). The second and more important aim is that the correlation plot presented in the upper panel of Figure 10 unequivocally shows that the reaction rate behavior in the Ce−Ti composite system is dominated by the availability of holes at the surface of the material. Toluene photodegradation has been shown to be a hole-triggered reaction.[57−59] Our results support this idea and, moreover, provide a quantitative analysis of it, indicating that the reaction rate is proportional to the number of such species available at the surface of the material. This provides strong evidence that the hole radical attack on the toluene molecule is

dx.doi.org/10.1021/cs400878b | ACS Catal. 2014, 4, 63−72

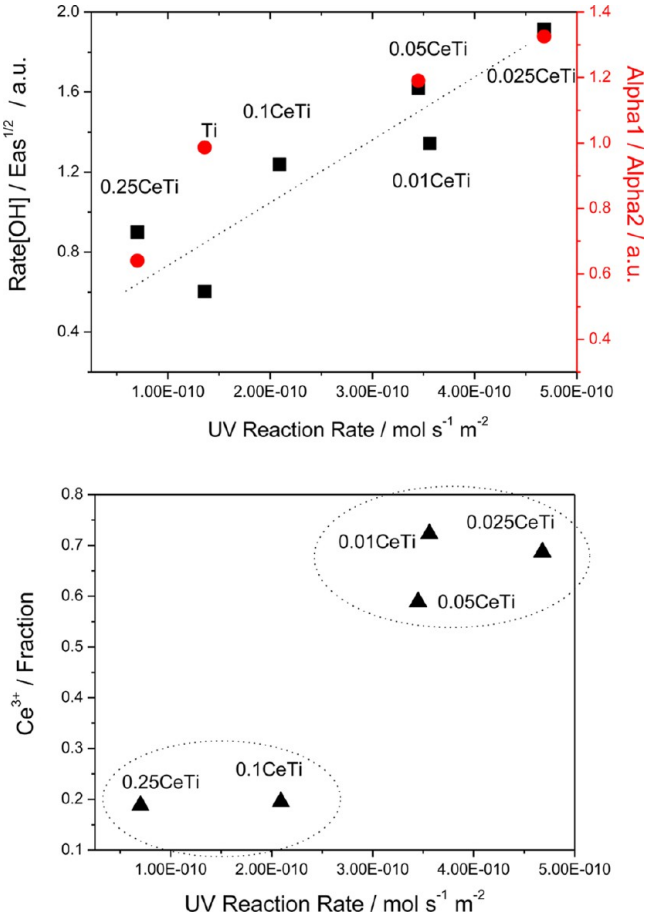

Figure 10. Upper panel: Correlation plot of the kinetic parameter ratio (eq 4) and the normalized rate of OH-related radical formation (eq 5) vs the reaction rate for the Ti reference and selected *x*CeTi samples. Lower panel: plot showing the correlation between the reaction rate and the Ce^{3+} fraction detected by XPS. Lines are guides for the eyes only.

a kinetically relevant step, which rationalizes photoactivity in the CeO_2–TiO_2 series and, particularly, the enhancement observed with respect to the bare titania reference system.

We can thus conclude that the contact between the ceria and titania influences the activity by promoting effective separation of charge and leaving hole species available for chemical reaction. This is not expected to be a simple effect of oxide–oxide (CeO_2–TiO_2) charge flow and separation due to band leveling effects between the corresponding conduction and valence bands of the bare ceria and titania. Although the ceria (valence/conduction) band position(s) and gap strongly depend on the preparation procedure, for our pure nano-CeO_2 (band gap of 2.55 eV),[32] the contact with titania would drive both types of charge species (electrons and holes) to the noneffective ceria surface,[4,60] neither promoting charge separation nor improving the effectiveness of the more photoactive surface, titania. Moreover, the presence of Ce^{3+} in a fluorite network is expected to further favor electron transfer and thus recombination if the effect in the conduction band position is exclusively considered.[4,60]

The correlation with the photoactivity displayed in the lower panel of Figure 10 still indicates that the presence of reduced Ce^{3+} appears to be key for interpreting the activity. As mentioned previously, Ce^{3+} states may alter the fluorite conduction band but also may allow the efficient location of TiO_2 conduction band electrons generated after photoexcitation. The corresponding electron trapping sites required to stabilize such charge species in the fluorite structure (more precisely, and as detailed below, at fluorite but near the ceria–titania interface) are unknown but would be related to the oxygen vacancies required to achieve charge neutrality in the presence of reduced Ce states.[53] The lower panel in Figure 10 indicates that the presence of Ce^{3+} states/oxygen vacancies divides the Ce–Ti composite samples in two groups. It appears that the samples producing relatively small quantities of hole-related radicals contain relatively small factions of reduced Ce states (below 20 atom % at the surface), while larger amounts of such radical species seem to correlate with larger fractions (above 50 atom %). We can thus suggest that the adequate Ce^{3+}/Ce^{4+} ratio is important to interpret the activity or, in other words, the fluorite structure presumably plays a role in the behavior of reduced Ce and/or oxygen vacancy sites. It has been shown that oxygen vacancies alter their electron-capturing properties as a function of their isolated or associated nature and that such nature is a function of the ceria primary particle size and other morphological variables.[48,53,61] The analysis of such an issue requires a rather sophisticated approach in order to track exclusively Ce–Ti-interface-related related oxygen vacancies and also to study the physicochemical properties of such entities. For now, we again recall that the stability of reduced Ce^{3+} states and the concominant presence of oxygen vacancies is intimately connected with the Ce–Ti interface.[49] In our case, the interface effect promotes the presence of the reduced Ce states by at least a factor of ca. 12.5 (considering the effect of titania in ceria particles around 8–10 nm).

We finish by mentioning that the morphological properties of the Ce–Ti composite samples only evolve very smoothly through the series (see previous subsection). Thus, a potential decrease in titania surface area available to the reactive mixture by a shadowing effect appears to be not determinant in explaining the behavior of the Ce–Ti composite samples as a function of the ceria content. A rough estimation considering the XRD-derived average particle size of ceria (Table 2) indicates that relative to 0.05CeTi there would be decays in activity of 6.3 and 12.9 times for 0.1CeTi and 0.25CeTi, respectively. As such numbers do not match the behavior presented in Figures 7 and 8, we can conclude that this issue has relatively low significance in interpreting the photoactivity trend observed in the sample series. Such a conclusion is in agreement with the previously described characterization of the samples as well as the outcome of the spectro-kinetic analysis.

IV. CONCLUSIONS

A series of CeO_2–TiO_2 materials containing ceria in a molar content from 1 to 25% were analyzed in the photoelimination of toluene. A complete structural and electronic characterization of the solids was obtained with the help of X-ray diffraction and electron paramagnetic resonance, UV–vis, and X-ray photoelectron spectroscopies as well as high-resolution transmission electron microscopy.

To interpret the behavior of the samples with respect to the single TiO_2 reference and also as a function of the ceria content, we have developed a novel spectro-kinetic approach where a joined analysis of the kinetics of the reaction and the fate of charge charriers is merged with mathematical modeling of the light–catalyst(s) interaction at the photoreactor. This produces a self-consistent approach that simultaneously validates the kinetic model and interprets the photoactivity.

dx.doi.org/10.1021/cs400878b | ACS Catal. 2014, 4, 63–72

The analysis has provided conclusive evidence for the critical role of the CeO_2−TiO_2 interface. A quasi-linear correlation was observed between the rate of surface-available hole-related species and the rate of toluene photoelimination. This provides a robust proof concerning the leading role of the oxide−oxide interface in charge separation and hole availability for toluene photodegradation at the surface of the materials. The physicochemical characterization suggests that this can be connected and favored by the presence of electron-capturing oxygen-vacancy-related centers, which in turn are stabilized by an oxide−oxide interface effect. The development of the spectro-kinetic approach and the use of the quantitative links between the derived observables allowed us to establish a rational platform to interpret the key variables of the photodegradation of toluene and the series behavior as a function of the Ce content of the material.

■ ASSOCIATED CONTENT

Supporting Information

Complete description of the photocatalytic measurements as well as the theoretical framework for interpreting the kinetic behavior of the materials. This material is available free of charge via the Internet at http://pubs.acs.org.

■ AUTHOR INFORMATION

Corresponding Authors

*E-mail: ak@icp.csic.es (A.K.).
*E-mail: mfg@icp.csic.es (M.F.-G.).

Notes

The authors declare no competing financial interest.

■ ACKNOWLEDGMENTS

A.K. and M.J.M.-B. thank MINECO for support through the postdoctoral "Ramón y Cajal" and predoctoral FPI programs, respectively. M.N.G.-C. also acknowledges financial support by UAM. Financial support by MINECO (Project CTQ2010-14872/BQU) is also acknowledged. Drs. Marco di Michiel and Laura Pascual are also thanked for measurements on beamline ID15 at ESRF and the HRTEM apparatus, respectively.

■ REFERENCES

(1) Hoffman, M. R.; Martin, S. T.; Choi, W.; Bahneman, D. W. *Chem. Rev.* **1995**, *95*, 69−121.
(2) Carp, O.; Huisan, C. L.; Reller, A. *Prog. Solid State Chem.* **2004**, *32*, 33−145.
(3) Thu, H.; Karkmaz, M.; Puzenat, E.; Guillard, C.; Herrmann, J. M. *Res. Chem. Intermed.* **2005**, *31*, 449−543.
(4) Kubacka, A.; Colón, G.; Fernández-García, M. *Chem. Rev.* **2012**, *112*, 1555−1614.
(5) Ohno, T.; Miyamoto, Z.; Nishijima, K.; Kanemitsu, H.; Xueyuan, F. *Appl. Catal., A* **2006**, *302*, 62−68.
(6) Li, Q.; Xie, R.; Mintz, E. A.; Shang, J. K. *J. Am. Ceram. Soc.* **2007**, *90*, 3863−3868.
(7) Kubacka, A.; Bachiller-Baeza, B.; Colón, G.; Fernández-García, M. *J. Phys. Chem. C* **2009**, *113*, 8553−8556.
(8) Kubacka, A.; Bachiller-Baeza, B.; Colón, G.; Fernández-García, M. *Appl. Catal., B* **2010**, *93*, 274−281.
(9) Kubacka, A.; Colón, G.; Fernández-García, M. *Appl. Catal., B* **2010**, *95*, 238−244.
(10) Yurdakal, S.; Augugliaro, V.; Loddo, V.; Palmisano, G.; Palmisano, L. *New J. Chem.* **2012**, *36*, 1762−1768.
(11) Huan, J.; Weng, S.; Lin, J. *J. Nat. Gas. Chem.* **2012**, *4*, 568−572.
(12) Gao, H.; Lu, B.; Liu, F.; Liu, Y.; Zhao, X. *Int. J. Photoenergy* **2012**, No. 453018.
(13) Menéndez-Flores, V.; Bahnemann, D. W.; Ohno, T. *Appl. Catal., B* **2011**, *103*, 99−108.
(14) Lai, C. W.; Sreekantan, S. *J. Alloys Compd.* **2013**, *547*, 43−50.
(15) Hidalgo, M. C.; Maicu, M.; Navío, J. A.; Colón, G. *J. Phys. Chem. C* **2009**, *113*, 12840−12846.
(16) Augugliaro, V.; Yurdakal, L.; Loddo, V.; Palmisano, G.; Palmisano, L. *Adv. Chem. Eng.* **2009**, *20*, 1−35.
(17) Colón, G.; Murcia López, S.; Hidalgo, M. C.; Navío, J. A. *Chem. Commun.* **2010**, *46*, 4809−4811.
(18) Balu, A. M.; Baruwati, B.; Serrano, E.; Cot, J.; García-Martínez, J.; Varma, R. S.; Luque, R. *Green Chem.* **2011**, *13*, 2750−2758.
(19) Kim, M. J.; Kim, K.-D.; Seo, H.-D.; Luo, Y.; Dey, N. K.; Kim, Y. D. *Appl. Surf. Sci.* **2011**, *258*, 2489−2499.
(20) Dey, N. K.; Kim, M. J.; Kim, K.-D.; Lee, K. H. *J. Mol. Catal. A: Chem.* **2011**, *337*, 33−38.
(21) Zhou, X.; Li, X.; Zhao, Q.; Liu, S. *J. Colloid Interface Sci.* **2012**, *383*, 13−18.
(22) Nair, R. G.; Roy, J. K.; Samdarshi, S. K.; Mukherjee, A. K. *Sol. Energy Mater. Sol. Cells* **2012**, *105*, 103−108.
(23) Iwaszu, K.; Nolan, M. *Catal. Sci. Technol.* **2011**, *3*, 2000−2008.
(24) Pérez-Larios, A.; López, R.; Hernández-Gordillo, A.; Tzompantzi, F.; Gómez, R.; Torres-Guerra, L. M. *Fuel* **2012**, *100*, 139−143.
(25) Kamat, P. V. *J. Phys. Chem. C* **2007**, *111*, 2834−2867.
(26) Kubacka, A.; Ferrer, M.; Martínez-Arias, A.; Fernández-García, M. *Appl. Catal., B* **2008**, *84*, 87−93.
(27) Taylor, M.; Ndifor, E. N.; Garcia, T.; Solsona, B.; Carley, A. F.; Taylor, S. H. *Appl. Catal., A* **2008**, *350*, 63−70.
(28) Hidalgo, M. C.; Murcia, M.; Navío, J. A.; Colón, G. *J. Mol. Catal. A: Chem.* **2011**, *397*, 112−120.
(29) Wen, Z.; Wu, W.; Liu, Z.; Zheng, H.; Li, J.; Chen, J. *Phys. Chem. Chem. Phys.* **2013**, *15*, 6773−6778.
(30) Jose, J.; Sorensen, C. M.; Rayclu, S. S.; Shersta, K. M.; Klabunde, J. *Int. J. Photoenergy* **2013**, No. 685614.
(31) Hernández-Alonso, M. D.; Hungría, A. B.; Martínez-Arias, A.; Fernández-García, M.; Coronado, J. M.; Conesa, J. C.; Soria, J. *Appl. Catal., B* **2004**, *50*, 167−175.
(32) Hernández-Alonso, M. D.; Hungría, A. B.; Martínez-Arias, A.; Coronado, J. M.; Conesa, J. C.; Soria, J.; Fernández-García, M. *Phys. Chem. Chem. Phys.* **2004**, *6*, 3524−3529.
(33) Ji, P.; Zhang, J.; Chen, F.; Anpo, M. *Appl. Catal., B* **2009**, *85*, 148−154.
(34) Parasupree, S.; Suzuki, Y.; Prisa-Art, S.; Yoshikawa, S. *J. Solid State Chem.* **2005**, *178*, 128−134.
(35) Li, G.; Zhang, D.; Yu, Y. C. *Phys. Chem. Chem. Phys.* **2009**, *11*, 3775−3782.
(36) Lin, H.; Wang, M.; Wang, Y.; Liang, Y.; Cao, W.; Su, Y. *J. Photochem. Photobiol., A* **2011**, *223*, 157−162.
(37) Wang, Y.; Li, B.; Zhang, C.; Cui, L.; Kang, S.; Li, X.; Zhou, L. *Appl. Catal., B* **2013**, *130−131*, 277−284.
(38) Muñoz-Batista, M. J.; Kubacka, A.; Gómez-Cerezo, M. N.; Tudela, D.; Fernández-García, M. *Appl. Catal., B* **2013**, *140−141*, 625−635.
(39) Fuerte, A.; Hernández-Alonso, M. D.; Maira, A. J.; Martínez-Arias, A.; Fernández-García, M.; Conesa, J. C.; Soria, J. *Chem. Commun.* **2001**, 2718−2719.
(40) Fuerte, A.; Hernández-Alonso, M. D.; Maira, A. J.; Martínez-Arias, A.; Fernández-García, M.; Conesa, J. C.; Soria, J. *J. Catal.* **2002**, *212*, 1−12.
(41) De Gennes, P. G.; Taupin, C. *J. Phys. Chem.* **1982**, *86*, 2294−2303.
(42) Fernández-García, M.; Wang, X.; Belver, C.; Hanson, J. C.; Rodriguez, J. A. *J. Phys. Chem. C* **2007**, *111*, 674−682.
(43) Williamson, G. K.; Hall, W. H. *Acta Metall.* **1953**, *1*, 22−31.
(44) Paparazzo, E. *Mater. Res. Bull.* **2011**, *46*, 323−326.
(45) Achery, S. N.; Sali, S. K.; Kulkarni, N. K.; Krishna, P. S. R.; Shinde, A. B.; Tyagi, A. K. *Chem. Mater.* **2009**, *21*, 5848−5859.

(46) Morgensen, M. In *Catalysis by Ceria and Related Materials*; Trovarelli, A., Ed.; Imperial College Press: London, 2002; pp 453−482.
(47) Wagner, C. D.; Riggs, W. M.; Davis, L. E.; Moulder, J. F. *Handbook of X-ray Photoemission Spectra*; Muilenberg, G. E., Ed.; Perkin-Elmer: Eden Prairie, MN, 1976.
(48) Lorschen, C.; Bromley, S. T.; Neyman, K. M.; Illas, F. *J. Phys. Chem. C* **2007**, *111*, 10142−10145.
(49) Johnston-Peck, A. C.; Senanayake, S. D.; Plata, J. J.; Kundu, S.; Xu, W.; Barrio, L.; Graciani, J.; Sanz, J. F.; Navarro, R. M.; Fierro, J. L. G.; Stach, E. A.; Rodriguez, J. A. *J. Phys. Chem. C* **2013**, *117*, 14463−14471.
(50) Tkuchibata, S. V. N.; Karakoti, A. S.; Baer, D. R.; Sumadrala, S.; Seal, S. *J. Phys. Chem. C* **2012**, *116*, 14108−14114.
(51) Palummo, M.; Giorgi, G.; Chiodo, L.; Rubio, A.; Yamashita, K. *J. Phys. Chem. C* **2012**, *116*, 18495−18503.
(52) Tsunekawa, S.; Fukuda, T.; Kasuya, A. *J. Appl. Phys.* **2000**, *87*, 1318−1323.
(53) Fernández-García, M.; Martínez-Arias, A.; Hanson, J. C.; Rodríguez, J. A. *Chem. Rev.* **2004**, *104*, 4063−4104.
(54) Grela, M. A.; Coronel, M. E. J.; Colussi, A. J. *J. Phys. Chem.* **1996**, *100*, 16940−16945.
(55) Janzen, E. G.; Sankuratry, N.; Kotake, Y. *J. Magn. Reson.* **1996**, *111*, 254−262.
(56) Chen, Q.; Shi, H.; Li, W. S.; Xu, Y.; Wu, D. W. *Catal. Sci. Technol.* **2012**, *2*, 1213−1220.
(57) d'Hennezel, O.; Pichat, P.; Ollis, D. F. *J. Photochem. Photobiol., A* **1998**, *118*, 197−204.
(58) Coronado, J. M.; Soria, J. *Catal. Today* **2007**, *123*, 37−41.
(59) Sleiman, M.; Conchon, P.; Ferronato, C.; Chovelon, J.-M. *Appl. Catal., B* **2009**, *86*, 159−165.
(60) Xu, Y.; Schoonen, M. A. A. *Am. Mineral.* **2000**, *85*, 543−556.
(61) Migani, A.; Vassylov, G. N.; Bromley, S. T.; Illas, F.; Neyman, K. M. *Chem. Commun.* **2010**, *46*, 5936−5938.